PNAS RESEARCH ARTICLE | BIOCHEMISTRY OPEN ACCESS

# Human lncRNA *RMRP* interacts with DEAD-box helicases and modulates mitochondrial function

Higor Sette Pereira[a], Jason Luddu[a], Govardhan Reddy Veerareddygari[a], Shridhar Kiran Sanghvi[b], Priyanshi B. Patel[a], Zachary E. Robinson[a], M. Quadir Siddiqui[a], Harpreet Singh[b], and Trushar R. Patel[a,c,d,1]

Edited by Janosch Hennig, European Molecular Biology Laboratory, Heidelberg, Germany; received August 15, 2025; accepted January 16, 2026 by Editorial Board Member James L. Manley

**The human long noncoding RNA (lncRNA) *RMRP*, initially identified as part of the RNase MRP complex, is linked to various human diseases. However, its structural flexibility and broader cellular roles are not well understood. Here, we offer a comprehensive analysis of *RMRP*'s structure in solution, its interactions with human proteins, and its mitochondrial functions. Using small-angle X-ray scattering (SAXS), we show that *RMRP* adopts different $Mg^{2+}$-dependent shapes, shifting from an extended Y-shaped form to a more compact one as $Mg^{2+}$ levels increase. We identified and characterized interactions between *RMRP* and the DEAD-box RNA helicases DDX5 and DDX3X, with DDX5 binding strongly and exhibiting ATP-dependent helicase activity on *RMRP*, while DDX3X mainly acts as an expression regulator. Both helicases are crucial for the proper mitochondrial localization of *RMRP*, working within a complex regulatory network. Functionally, reducing *RMRP* levels disrupts mitochondrial stability, leading to membrane depolarization and an increase in reactive oxygen species, without affecting cell growth. Mechanistically, *RMRP* specifically controls nuclear-encoded mitochondrial proteins involved in cristae structure (DNAJC11) and respiratory chain function (NDUFS8). Our results position *RMRP* as a structurally adaptable lncRNA that collaborates with RNA helicases to preserve mitochondrial health through specific gene regulation. These insights provide perspectives on *RMRP*'s biology and the molecular mechanisms underlying *RMRP*-related disorders, which could inform future therapies for conditions resulting from *RMRP* dysfunction.**

RMRP | long noncoding RNA | DEAD-box helicases | mitochondrial function

## Significance

*RMRP* adopts distinct $Mg^{2+}$-dependent conformations and interacts with DEAD-box helicases DDX5 and DDX3X, which display different binding affinities and unwinding activities. DDX5 and DDX3X are crucial for *RMRP* mitochondrial localization and function within a regulatory network, with DDX3X acting as a key upstream regulator of *RMRP* expression. *RMRP* plays a key role in maintaining mitochondrial health and supporting bioenergetic functions.

Long noncoding RNAs (lncRNAs) have emerged as crucial regulators of gene expression and cellular function, often operating through complex structural dynamics and interactions with diverse protein partners (1). Among these, the RNA component of mitochondrial RNA processing endoribonuclease (*RMRP*) represents one evolutionarily conserved and functionally intriguing lncRNA in the human genome (2). Originally identified as a component of the RNase MRP complex involved in mitochondrial RNA processing and ribosomal RNA maturation, *RMRP* has since been implicated in a wide range of cellular processes and human diseases (3, 4). *RMRP* is a 268-nucleotide lncRNA encoded by the *RMRP* gene, located on chromosome 9p13.3. Mutations in *RMRP* cause cartilage-hair hypoplasia (CHH), an autosomal recessive disorder characterized by short stature, sparse hair, immune deficiency, and increased predisposition to certain cancers (3). Beyond its role in CHH, *RMRP* dysregulation has been associated with various cancers, including breast, lung, and colorectal cancers, where it often exhibits elevated expression and correlates with poor prognosis (5–7).

The canonical role of *RMRP* involves its association with protein components to form the RNase MRP complex, which participates in mitochondrial RNA processing, rRNA maturation, and cell cycle regulation by degrading specific mRNAs (8, 9). However, emerging evidence suggests that *RMRP* has functions beyond this complex, potentially including roles in telomerase regulation, microRNA processing, and mitochondrial DNA replication (10–12). These diverse activities likely depend on specific interactions with various proteins, many of which remain to be identified and characterized. The subcellular localization of *RMRP* is another important aspect of its function. While initially described as primarily nucleolar, *RMRP* has been detected in both nuclear and mitochondrial compartments (13). The mechanisms governing *RMRP* trafficking between cellular compartments and how this compartmentalization relates to its various functions remain somewhat unknown. Despite its clinical significance, the structural characteristics and molecular mechanisms underlying *RMRP*'s diverse functions remain incompletely understood. While

Author affiliations: [a]Alberta RNA Research and Training Institute, Department of Chemistry and Biochemistry, University of Lethbridge, Lethbridge, AB T1K 3M4, Canada; [b]Department of Physiology and Cell Biology, College of Medicine, The Ohio State University, Columbus, OH 43210; [c]Li Ka Shing Institute of Virology and Discovery Lab, Faculty of Medicine and Dentistry, University of Alberta, Edmonton, AB T6G 2E1, Canada; and [d]Department of Microbiology, Immunology and Infectious Diseases, Cumming School of Medicine, University of Calgary, Calgary, AB T2N 4N1, Canada

Author contributions: H.S.P., G.R.K., S.K.S., H.S., and T.R.P. designed research; H.S.P., J.L., G.R.V., S.K.S., P.B.P., Z.E.R., M.Q.S., and T.R.P. performed research; H.S.P., J.L., G.R.V., S.K.S., Z.E.R., M.Q.S., and T.R.P. analyzed data; and H.S.P., J.L., G.R.V., S.K.S., and T.R.P. wrote the paper.

The authors declare no competing interest.

This article is a PNAS Direct Submission. J.H. is a guest editor invited by the Editorial Board.



[1]To whom correspondence may be addressed. Email: trushar.patel@uleth.ca.

This article contains supporting information online at https://www.pnas.org/lookup/suppl/doi:10.1073/pnas.2522583123/-/DCSupplemental.

Published February 20, 2026.

secondary structure predictions suggest a complex, branched architecture (9, 14), the three-dimensional conformation of *RMRP* and its potential structural dynamics under varying physiological conditions have not been experimentally determined.

DEAD-box helicases are a type of RNA helicase that play diverse roles in RNA metabolism and are direct regulators of RNA structures by unwinding it, forming duplex structures, separating RNA–protein complexes, and also functioning as assembly platforms for larger ribonucleoprotein complexes (15). DDX5 (DEAD-box helicase 5) and DDX3X (DEAD-box helicase 3) are closely related RNA helicases within the DEAD-box RNA helicase family, sharing structural and functional similarities. Both DDX5 and DDX3X regulate translation by influencing initiation and elongation processes, as well as impacting gene expression (16, 17). DDX3X facilitates mRNA export, and DDX5 enhances this activity, thereby aiding in the transport of mature mRNA for translation (18, 19). In the context of viral infections, they interact with viral RNA and proteins to modulate replication (20, 21). Dysregulation of DDX3X and DDX5 in cancer contributes to both gene expression and oncogenesis (19, 22). Additionally, DDX3X's role in innate immunity, coupled with its interaction with DDX5, influences immune-related gene expression and pathogen responses (20). These interactions emphasize the intricate nature of RNA metabolism and cellular processes, where multiple helicases and proteins cooperate to regulate gene expression and maintain cellular balance.

In this study, we conducted a comprehensive analysis of the *RMRP* structure, protein interactions, and mitochondrial functions. Using small-angle X-ray scattering (SAXS), we characterized the three-dimensional conformation of *RMRP* under different magnesium concentrations. Through proteomic approaches, we identified interactions between *RMRP* and the DEAD-box RNA helicases and characterized these interactions using biophysical and cellular assays. We further investigated how these helicases influence *RMRP* localization and expression, revealing a complex regulatory network. Finally, we examined the functional consequences of *RMRP* depletion on mitochondrial homeostasis and identified specific mitochondrial pathways regulated by *RMRP*. Our findings provide insights into the structural dynamics, protein interactions, and mitochondrial functions of *RMRP*, thereby advancing our understanding of this multifunctional lncRNA and establishing a foundation for future investigations into its roles in both normal cellular physiology and disease states.

## Results and Discussion

**Comprehensive Structural Characterization of *RMRP* in Solution.** In vitro transcribed *RMRP* was purified using size-exclusion chromatography (SEC). The elution profile indicates a purified RNA as visualized at $UV_{260}$ eluting as a monodisperse single peak from 10.5 to 12 mL on a Superdex 200 Increase GL 10/300 column (*SI Appendix*, Fig. S1*A*). *SI Appendix*, Fig. S1*B* illustrates the native gel for the *RMRP* peak fraction, indicating that the RNAs migrated closely superior to a 200-nucleotide control RNA, and between the 200 and 300 bp markers. In addition, we utilized multiangle light scattering (MALS) in line with SEC to evaluate the absolute molar mass of *RMRP* in solution. By measuring the refractive index (RI), light scattered (LS), and molar mass (MW), we were able to generate a representation of the results (*SI Appendix*, Fig. S1*C*). Calculations show that the absolute MW for *RMRP* in solution is approximately 92.89 kDa, which is in excellent agreement with the theoretical value (90.58 kDa). This demonstrates that the RNA is monodisperse and free from aggregation in solution. Exclusion of RNA degradation or shorter transcripts can be ensured, as no detectable smaller fragments were found.

We employed SAXS to gain structural insights into the shape of *RMRP* in solution. $Mg^{2+}$ promotes RNA conformational transitions at different concentrations (23) and has been shown to increase the structural compactness of human lncRNAs at higher concentrations (24–26). Therefore, we investigated the *RMRP* structure in buffers containing 5 and 20 mM of this cation. The datasets obtained from both *RMRP* conditions were combined to display the intensity of scattering as a function of angle (*SI Appendix*, Fig. S2*A*), and all quantitative data are represented in *SI Appendix*, Table S4. The linearity observed in the Guinier analysis (*SI Appendix*, Fig. S2*B*) demonstrates that *RMRP* samples are pure, monodisperse, and free of aggregation. Next, we presented the foldness of *RMRP* using Kratky analysis (*SI Appendix*, Fig. S2*C*) as well as every dataset was analyzed using paired-distance distribution [P(r)] (*SI Appendix*, Fig. S2*D*). P(r) indicates an elongated conformation for both RNAs (*SI Appendix*, Fig. S2*D*). The maximum distance ($D_{max}$) for each RNA was 230 Å at 5 mM $Mg^{2+}$ and 180 Å at 20 mM $Mg^{2+}$, indicating a less elongated structure at higher magnesium concentrations. DAMMIN was used to obtain 3D low-resolution structures through ab initio modeling for both 5 and 20 mM $Mg^{2+}$ conditions. A total of 20 models for each condition were generated, and their quality was demonstrated by the favorable agreement ($\chi^2$) of 1.30 and 1.16 for 5 and 20 mM $Mg^{2+}$, respectively (*SI Appendix*, Table S3). Models were filtered and averaged into a single representative using DAMAVER. The representative structure demonstrated a good fit with each model, as indicated by normalized spatial discrepancies (NSD) of approximately 1.20 and 1.12 (*SI Appendix*, Table S3).

In both conditions, *RMRP* is displayed in an elongated, asymmetric, and nonglobular shape (Fig. 1) (27), as commonly illustrated for other human lncRNAs (28–30). The surface structure of *RMRP*, at 5 mM $Mg^{2+}$, indicates a very elongated RNA (230 Å) with a protrusion forming a Y-shaped structure (purple, Fig. 1*A*). Alternatively, the 20 mM $Mg^{2+}$ highlights a less-extended structure (180 Å) with two bulges at the right end of the structure (red, Fig. 1*B*). These differences in *RMRP*'s structure upon the addition of $Mg^{2+}$ ions are consistent with previous structural studies of human lncRNA, such as *Braveheart* (26), *HOTAIR* (24), and *repA* (25). It is widely accepted that the presence of $Mg^{2+}$ exerts a notable influence on the conformations of larger RNA (greater than 206 kDa). In contrast, smaller RNAs (less than 69 kDa) exhibit only minor alterations in response to these divalent cations (26). Based on this classification, it can be argued that *RMRP* (~90 kDa) is neither a large nor a small RNA. Our SAXS models have demonstrated that a drastic structural alteration can be observed in *RMRP* by varying the $Mg^{2+}$ concentration (Fig. 1). Additionally, the sensitivity of an RNA's structure to $Mg^{2+}$ concentration is a strong indicator of the presence of tertiary interactions in the RNA (31, 32). However, the high-resolution structural characterization of *RMRP* has yet to be determined.

Previous research evaluated *RMRP*'s secondary structure using Selective 2′-hydroxyl acylation analyzed by primer extension (SHAPE) and PAIR-Map probing methods (33, 34). The secondary-structure profile is presented on the Rfam website, and an R-scape optimized structure is available (family RF00030). The *RMRP* structure observed in Rfam is extended and branched, resembling SAXS models (Fig. 1). SAXS can be used to obtain three-dimensional structures of molecules in their native state; however, it has lower resolution and cannot provide directional information. As previously demonstrated by our group (29), we employed a sophisticated approach that combines secondary

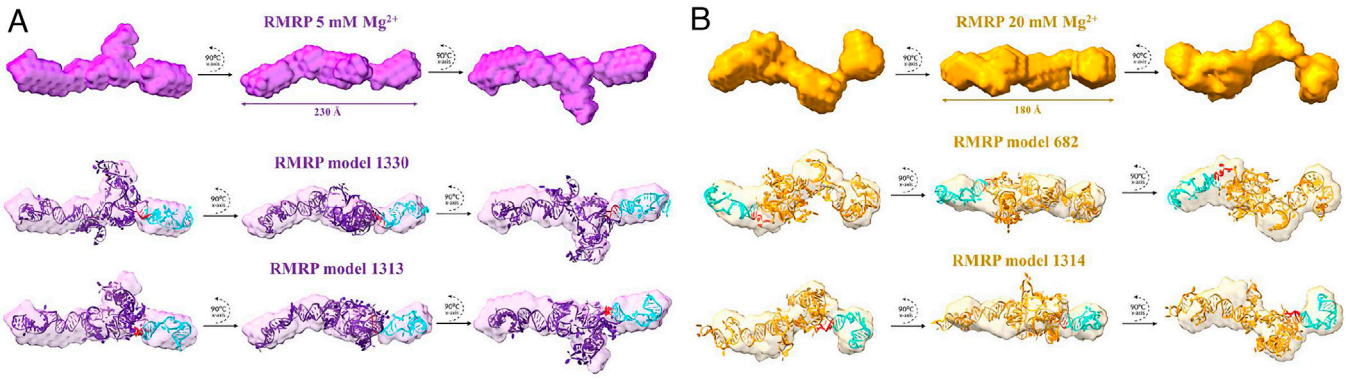


**Fig. 1.** SAXS envelope reconstructions and tertiary structure models of *RMRP* under different $Mg^{2+}$ conditions. (*A*) *RMRP* structure in 5 mM $Mg^{2+}$ (purple). *Top* row: SAXS-derived low-resolution envelope showing an elongated Y-shaped structure with a maximum dimension of 230 Å. *Middle* and *Bottom* rows: Two alternative tertiary structure models (1,330 and 1,313) fitted within the SAXS envelope, with RPP20–RPP25 binding regions highlighted in blue/cyan. (*B*) *RMRP* structure in 20 mM $Mg^{2+}$ (orange/gold). *Top* row: SAXS-derived envelope revealing a more compact structure with a maximum dimension of 180 Å and characteristic bulges. *Middle* and *Bottom* rows: Tertiary structure models (682 and 1,314) fitted within the SAXS envelope, showing the RPP20–RPP25 binding regions in the same coloring scheme. The higher $Mg^{2+}$ concentration induces significant conformational changes while maintaining the overall secondary structure elements and accessibility of protein-binding interfaces. In blue is highlighted the RPP20–RPP25 binding region, whereas the complementary region used for the helicase assay is in red (Fig. 2 *C* and *D*).

structure with SAXS to generate computational tertiary structures. Tertiary structure models of *RMRP* reveal its structural dynamics and functional implications across varying $Mg^{2+}$ concentrations. At 5 mM $Mg^{2+}$, models 1,313 and 1,330 (Fig. 1*A*) show an extended conformation with characteristic branching, aligning with the Y-shaped SAXS envelope. The RPP20–RPP25 binding site [in blue, obtained from Yin et al. (35)] is prominently exposed, suggesting an accessible surface for protein complex formation during RNase MRP assembly. In contrast, the 20 mM $Mg^{2+}$ condition (models 682 and 1,314, Fig. 1*B*) reveals a compact structure, reducing the overall length to about 180 Å. Although the RPP20–RPP25 binding site remains solvent-accessible, it is reoriented in this more condensed state. The higher $Mg^{2+}$ concentration reorganizes. This comparison indicates that increasing $Mg^{2+}$ from 5 to 20 mM results in significant tertiary rearrangements, reflecting different functional states of *RMRP*. Moreover, models at 20 mM $Mg^{2+}$ reveal potential long-range tertiary interactions enhancing structural stability. Notably, the RPP20–RPP25 binding region maintains its integrity across various conditions, indicating its robustness and biological significance in ensuring functional protein binding under different cellular conditions, thereby supporting *RMRP*'s role in RNase MRP formation.

***RMRP* Expression Varies Across Different Cell Lines.** To investigate the functional relevance of *RMRP* in cellular contexts, we first examined its expression levels across various human cell lines. Quantitative RT-PCR analysis revealed striking differences in *RMRP* expression patterns among the cell lines tested (Fig. 2*A*). The prostate cancer metastatic cell line PC-3 M exhibited exceptionally high *RMRP* expression, approximately 4.7-fold higher than that of the housekeeping gene β-actin. This was followed by substantial expression in Huh-7 hepatocellular carcinoma cells (4.2-fold) and moderate expression in A549 lung adenocarcinoma cells (2.4-fold) and SH-SY5Y neuroblastoma cells (2.3-fold). In contrast, HEK293 embryonic kidney cells showed baseline *RMRP* expression levels comparable to β-actin.

The differential expression of *RMRP* across these cell lines is particularly intriguing, given *RMRP*'s established roles in mitochondrial homeostasis, ribosomal RNA maturation, and cell cycle regulation (36, 37). The significantly elevated expression in PC-3 M cells is consistent with recent studies suggesting that *RMRP* upregulation correlates with cancer progression and metastatic potential (38, 39). These findings align with reports that *RMRP* can function as an oncogenic long noncoding RNA (lncRNA) in several cancer types, including prostate cancer (38, 40). Based on these expression profiles and the limited literature on *RMRP*'s role in prostate cancer, we selected PC-3 M cells for subsequent analyses to explore the molecular interactions and functional significance of *RMRP* in this context.

***RMRP* Interacts With a Network of RNA-Binding Proteins.** To elucidate the molecular mechanisms underlying *RMRP*'s biological functions, we performed RNA pull-down assays followed by mass spectrometry to identify proteins that interact with *RMRP* in PC-3 M cells. Gene Ontology (GO) analysis of the identified proteins revealed significant enrichment in several biological pathways (Fig. 2*B*). As expected, ribosome biogenesis (29.5-fold enrichment) and RNA regulation and splicing (21.7-fold enrichment) were among the most significantly enriched processes, confirming *RMRP*'s canonical roles in RNA processing (37, 41). Additionally, oxidative phosphorylation showed substantial enrichment (22.3-fold), consistent with *RMRP*'s known involvement in mitochondrial function (13, 42). Interestingly, our analysis also identified significant associations with various neurological and metabolic disorders, including Parkinson's disease, Alzheimer's disease, amyotrophic lateral sclerosis, and diabetic cardiomyopathy. These associations suggest previously unexplored roles for *RMRP* in neurodegenerative processes and metabolic regulation. Such connections have been hinted at in recent studies linking mitochondrial RNA processing defects to neurodegeneration (43, 44), but our data provide direct evidence for *RMRP*'s potential involvement in these pathways.

Further analysis of the protein interactome revealed that *RMRP* associates with a complex network of RNA-binding proteins (RBPs) in PC-3 M cells (Fig. 2*C* and *SI Appendix*, Fig. S3). Notably, we identified interactions with two DEAD-box RNA helicases, DDX5 and DDX3X, which have not been previously reported as direct *RMRP* binding partners. These helicases are known to play crucial roles in RNA metabolism, including splicing, translation, and transport (45–47). The identification of DDX5 and DDX3X as *RMRP*-interacting proteins is particularly significant when considered alongside previously established *RMRP*-binding partners. Our STRING network analysis shows that DDX5 and DDX3X form a connected protein–protein

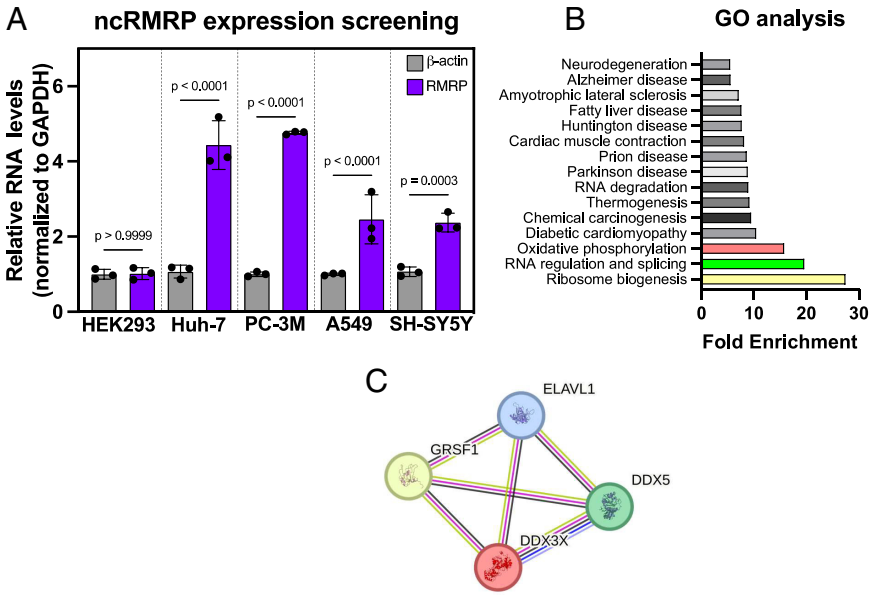


**Fig. 2.** *RMRP* expression profile and protein interaction analysis in human cell lines. (*A*) RT-qPCR analysis of *RMRP* expression across five human cell lines (HEK293, Huh-7, PC-3 M, A549, and SH-SY5Y) normalized to GAPDH. PC-3 M prostate cancer cells show the highest expression level (~4.7-fold), followed by Huh-7 hepatocellular carcinoma cells (~4.2-fold). β-actin expression is shown as a reference. Statistical significance was determined by one-way ANOVA with Dunnett's post hoc test (n = 3, biological replicates). (*B*) Gene Ontology (GO) enrichment analysis of proteins identified in the *RMRP* pull-down from PC-3 M cells. The three most significantly enriched biological processes (highlighted in color) include ribosome biogenesis (blue), RNA regulation and splicing (green), and oxidative phosphorylation (red). Several neurodegenerative and metabolic disorders also show significant enrichment. This analysis was performed using ShinyGO 0.77 with default settings. (*C*) STRING protein–protein interaction network of selected *RMRP*-binding proteins identified in this study (DDX3X and DDX5, highlighted) and their connections to previously reported *RMRP* interactors (ELAVL1/HuR and GRSF1). Line thickness indicates the strength of data support for each interaction.

interaction network with ELAV-like RNA binding protein 1 (ELAVL1, also known as HuR) and G-rich RNA sequence binding factor 1 (GRSF1) (Fig. 2*C*). Previous studies have demonstrated that HuR and GRSF1 interact with *RMRP* and influence its subcellular localization and function (13). HuR has been shown to modulate *RMRP*'s role in regulating mitochondrial RNA processing, while GRSF1 facilitates *RMRP* localization to mitochondria and promotes its interaction with mitochondrial RNAs.

**Direct Binding of DDX5 and DDX3X to *RMRP* ATP-Dependent Helicase Activity.** Following our identification of DDX5 and DDX3X as potential *RMRP*-interacting proteins, we sought to characterize these interactions in vitro using purified components. $DDX3X_{132\text{-}607}$ was purified according to previous protocols (48, 49). Additionally, a protocol for purifying DDX5 was developed, yielding a pure protein (*SI Appendix*, Fig. S4). Subsequently, we used purified proteins and RNA to characterize their interaction in vitro. MST analysis revealed that both RNA helicases directly bind to *RMRP* with distinct binding affinities (Fig. 3 *A* and *B*). DDX5 exhibited a strong interaction with *RMRP*, with a dissociation constant ($K_D$) of 1.38 ± 0.44 μM, indicating a high-affinity binding. In contrast, $DDX3X_{132\text{-}607}$ showed a more moderate affinity with a $K_D$ of 7.06 ± 2.49 μM. These binding characteristics were further confirmed by EMSAs, which demonstrated concentration-dependent complex formation between the helicases and *RMRP*. For DDX5, complex formation was clearly visible starting at 4 μM protein concentration, with nearly complete binding observed at 12 μM (*SI Appendix*, Fig. S5*A*). $DDX3X_{132\text{-}607}$ required higher concentrations to achieve similar levels of complex formation, with substantial shifts occurring at concentrations above 9 μM and increasing up to 22 μM (*SI Appendix*, Fig. S5*B*). DEAD-box helicases generally recognize RNA substrates through their conserved RecA-like helicase core domains. However, they exhibit structural and sequence preferences. DDX5 preferentially binds structured RNAs containing double-stranded regions and shows affinity for G-rich sequences (50, 51), while DDX3X recognizes relatively unstructured, purine-rich sequences and 5' UTR structures (52, 53).

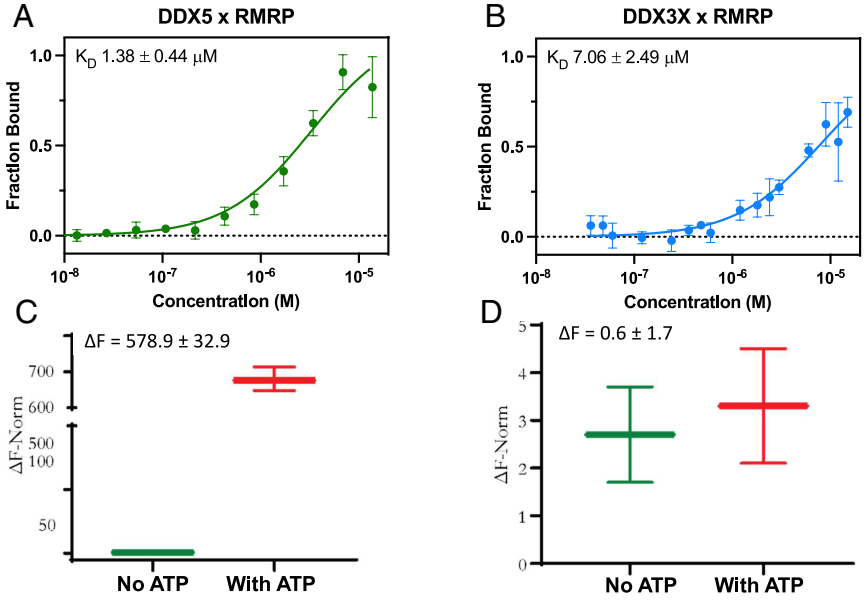


**Fig. 3.** Characterization of DDX5 and DDX3X interactions with *RMRP* and their helicase activities (*A*) Microscale thermophoresis (MST) analysis of DDX5 binding to *RMRP*, showing a concentration-dependent binding curve with a high-affinity interaction (KD = 1.38 ± 0.44 μM). Data points represent mean ± SD from three independent experiments. (*B*) MST analysis of DDX3X binding to *RMRP*, revealing a moderate-affinity interaction (KD = 7.06 ± 2.49 μM), approximately fivefold weaker than DDX5. Data points represent mean ± SD from three independent experiments. (*C*) ATP-dependent helicase activity of DDX5 on *RMRP* structure, measured using fluorescently labeled DNA oligonucleotides complementary to *RMRP* double-stranded regions. A substantial increase in normalized fluorescence (ΔF = 578.9 ± 32.9) is observed in the presence of ATP (red) compared to its absence (green), indicating strong unwinding activity. (*D*) Helicase activity of DDX3X on *RMRP* structure under the same conditions, showing minimal ATP-dependent activity (ΔF = 0.6 ± 1.7), suggesting that DDX3X does not efficiently unwind *RMRP* secondary structure in vitro.

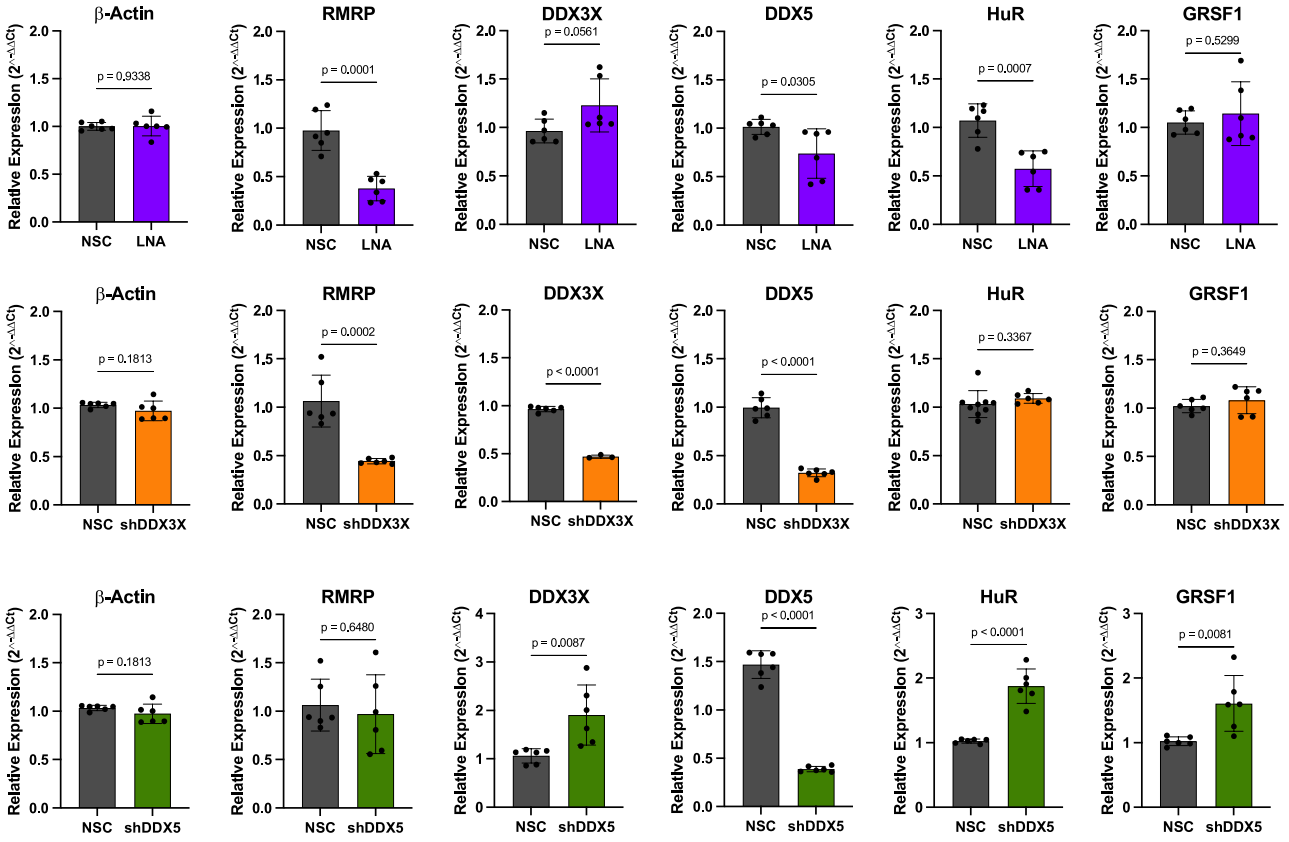


**Fig. 4.** Regulatory network analysis through targeted knockdown of *RMRP* and associated RNA helicases. Quantitative RT-PCR analysis of expression levels following targeted knockdowns in PC-3 M cells. All values are normalized to GAPDH and presented relative to nonsilencing control (NSC). *Top* panel: Effects of *RMRP* knockdown using locked nucleic acid (LNA) antisense oligonucleotides on the expression of network components. *RMRP* depletion significantly reduces DDX5 and HuR expression while slightly increasing DDX3X levels. *Middle* panel: Consequences of DDX3X knockdown using shRNA, showing substantial reduction in both *RMRP* and DDX5 expression without significant effects on HuR or GRSF1 levels. *Bottom* panel: Effects of DDX5 knockdown, which triggers compensatory upregulation of DDX3X, HuR, and GRSF1 while maintaining *RMRP* expression. Data are presented as mean ± SD from three independent experiments. Statistical significance was determined by unpaired *t* test comparing each knockdown to its corresponding NSC (*$P < 0.05$). These results reveal a complex regulatory network where DDX3X functions as a key upstream regulator of *RMRP*, while DDX5 depletion activates compensatory mechanisms to maintain network function.

Analysis of *RMRP*'s secondary structure reveals both features: well-defined hairpin structures that could serve as DDX5 binding sites and a prominent G-rich region that could represent a potential DDX3X recognition element (Fig. 3 *A* and *B*). Additionally, GRSF1 contains three GRSF (G-rich sequence factor) domains specifically evolved to recognize G-rich RNA sequences, consistent with its interaction with *RMRP*'s G-rich region.

To determine whether DDX5 and $DDX3X_{132\text{-}607}$ can modulate *RMRP* structure through their helicase activity, we performed helicase assays using fluorescently labeled DNA oligonucleotides complementary to double-stranded regions of *RMRP* (see *SI Appendix*, for *Materials and Methods*). As shown in Fig. 3*C*, DDX5 exhibited strong ATP-dependent helicase activity on *RMRP* structure, with a significant increase in normalized fluorescence ($\Delta F = 578.9 \pm 32.9$) in the presence of ATP compared to minimal activity in its absence. This substantial difference indicates that DDX5 can efficiently unwind *RMRP*'s secondary structure in an ATP-dependent manner, consistent with its known role as a processive RNA helicase (54). In contrast, $DDX3X_{132\text{-}607}$ showed very little ATP-dependent helicase activity on *RMRP* structure (Fig. 4*D*). The difference in fluorescence between ATP-present and ATP-absent conditions ($\Delta F = 0.6 \pm 1.7$) was minimal and statistically insignificant, suggesting that $DDX3X_{132\text{-}607}$ may not function as an active helicase on *RMRP* under these experimental conditions. This result is somewhat unexpected, given the established helicase activity of $DDX3X_{132\text{-}607}$ on other RNA substrates (48, 49). Still, it could indicate substrate specificity or a requirement for additional cofactors not present in our in vitro system. The striking difference in helicase activity between DDX5 and DDX3X on *RMRP* structure has important implications for understanding their respective roles in *RMRP* biology. DDX5's strong ATP-dependent unwinding activity suggests it may function to remodel *RMRP*'s secondary structure, potentially facilitating interactions with other proteins or exposing specific regions required for *RMRP*'s various cellular functions. DDX5 could serve as a cellular factor that actively promotes specific structural transitions in *RMRP*. On the other hand, the limited helicase activity of $DDX3X_{132\text{-}607}$ on *RMRP* suggests it may play a different role in *RMRP* function. Rather than actively unwinding the *RMRP* structure, DDX3X might serve as a binding partner that stabilizes specific *RMRP* conformations or facilitates interactions with other proteins in the *RMRP* ribonucleoprotein complex. These findings align with emerging evidence suggesting that DEAD-box helicases can have diverse effects on lncRNA structure and function, extending beyond their simple unwinding activity (15). For instance, DDX5 has been shown to facilitate structural rearrangements in other long noncoding RNAs (lncRNAs), such as *MALAT1*, contributing to their functions at nuclear phosphorylation sites and in pre-mRNA splicing, respectively (55). Similarly, DDX3X has been implicated in regulating the function of lncRNAs involved in immune responses and cancer progression (56).

**Gene Expression Analysis of the *RMRP* and Helicases Network.** To elucidate the functional relationships within the *RMRP*-associated protein network, we performed targeted knockdown studies of

*RMRP*, DDX3X, and DDX5 and assessed their impact on the expression of each other as well as known *RMRP*-interacting proteins HuR and GRSF1 (Fig. 4). *RMRP* knockdown using locked nucleic acid (LNA) antisense oligonucleotides resulted in a significant reduction of *RMRP* levels to approximately 30% of control levels. DDX3X expression showed a modest, not significant increase ($P$ = 0.056). In contrast, both DDX5 and HuR levels were substantially decreased, indicating that *RMRP* positively regulates their expression. GRSF1 expression remained relatively unchanged following *RMRP* knockdown. These findings reveal that *RMRP* not only interacts with these RNA-binding proteins but also modulates their expression, particularly DDX5 and HuR. The positive regulation of HuR by *RMRP* is especially intriguing as it suggests a feedback loop, given that HuR has been previously shown to stabilize *RMRP* and influence its subcellular localization (13).

Knockdown of DDX3X (middle panel, Fig. 4) resulted in dramatic changes to the expression pattern of the entire network. Most notably, *RMRP* levels were reduced to approximately 40% of control levels, indicating that DDX3X is essential for maintaining normal *RMRP* expression. This finding is particularly significant as it establishes a regulatory role for DDX3X in *RMRP* biology, extending beyond its direct binding interaction demonstrated in our earlier experiments (Fig. 3*B*). DDX5 expression was also markedly reduced following DDX3X knockdown, suggesting that DDX3X positively regulates DDX5 expression. Interestingly, neither HuR nor GRSF1 expression was significantly affected by DDX3X depletion. This selective effect on DDX5, but not on other *RMRP*-binding proteins, indicates that DDX3X regulation is specific rather than a general impact on RNA-binding proteins. The substantial decrease in *RMRP* levels following DDX3X knockdown provides important functional context for our earlier observation that DDX3X binds *RMRP* with moderate affinity but exhibits minimal helicase activity (Fig. 4 *B* and *D*). Rather than directly modulating *RMRP* structure through unwinding activity, DDX3X appears to function primarily as a regulator of *RMRP* expression. This regulatory role may involve multiple mechanisms, including transcriptional regulation, modulation of RNA stability, or indirect effects through other factors within the network. Recent studies have implicated DDX3X in the regulation of various long noncoding RNAs (lncRNAs) in cancer cells (18, 56). Our findings extend this regulatory role to *RMRP*, suggesting that DDX3X may be a central regulator of noncoding RNA networks in cancer.

In contrast, depletion of DDX5 (Fig. 4, *Bottom* panel) had minimal impact on *RMRP* expression (Fig. 3 *A* and *C*). This suggests that DDX5 is not essential for maintaining *RMRP* levels, although it may still influence *RMRP* function through direct structural modulation, as indicated by our helicase assays. Surprisingly, DDX5 knockdown resulted in a significant upregulation of DDX3X, HuR, and GRSF1 expression. This coordinated upregulation of multiple *RMRP*-binding partners suggests a compensatory mechanism that may serve to maintain *RMRP* function when DDX5 is depleted. The differential responses to DDX5 versus DDX3X knockdown highlight their distinct roles in the *RMRP* regulatory network. DDX3X appears to function as an upstream regulator essential for maintaining *RMRP* expression. At the same time, DDX5 likely acts more directly on *RMRP* function through its helicase activity, with its loss triggering compensatory upregulation of other *RMRP*-binding partners. These compensatory changes following DDX5 knockdown align with emerging views of lncRNA regulation, which involve complex, interconnected networks rather than linear pathways (5758, 59). In the case of *RMRP*, our data suggest a regulatory network in which DDX3X serves as a key upstream regulator of *RMRP* expression. At the same time, DDX5, HuR, and GRSF1 form an interconnected system that might collectively modulate *RMRP* function through direct interactions. The upregulation of HuR and GRSF1 following DDX5 knockdown is particularly noteworthy given their established roles in *RMRP* biology. HuR has been shown to stabilize *RMRP* and regulate its function in mitochondrial RNA processing, while GRSF1 facilitates the localization of *RMRP* to mitochondria (13).

**DDX5 and DDX3X Differentially Regulate the Subcellular Localization of *RMRP*.** *RMRP* functions in multiple cellular compartments, with distinct roles in the nucleus, as part of the RNase MRP complex for pre-rRNA processing, and in mitochondria for mitochondrial RNA processing and DNA replication (37, 41). Previous studies have established that RNA-binding proteins HuR and GRSF1 influence *RMRP* trafficking, with GRSF1 specifically facilitating mitochondrial localization (13). Having established that DDX5 and DDX3X interact with *RMRP* and affect its expression network, we investigated whether these helicases also affect *RMRP*'s subcellular distribution. Using FISH assays with *RMRP*-specific probes (green) and MitoTracker to visualize mitochondria (red), we examined *RMRP* localization in control cells and cells with DDX5 or DDX3X knockdown (Fig. 5). In control cells (NSC, *Top* panel), *RMRP* displayed a clear distribution pattern with both nuclear localization (purple arrows) and distinct mitochondrial colocalization (orange arrows) visible as yellow-orange signals in the merged images. This dual localization is consistent with *RMRP*'s established roles in both compartments (13). Surprisingly, knockdown of either DDX5 (middle panel) or DDX3X (*Bottom* panel) resulted in a marked reduction in mitochondrial *RMRP* localization. In both knockdown conditions, the colocalization between *RMRP* and MitoTracker (indicated by orange arrows) was substantially diminished compared to control cells. In contrast, nuclear signals (indicated by purple arrows) remained detectable. Notably, in DDX3X-depleted cells, mitochondrial morphology appeared altered, with a more fragmented and dispersed pattern compared to the organized network in control cells, suggesting potential mitochondrial dysfunction associated with reduced mitochondrial *RMRP* levels. Quantitative colocalization analysis using the Pearson correlation coefficient (PCC) and Manders coefficients confirmed these visual observations. Control cells showed robust *RMRP*-mitochondria colocalization (PCC = 0.68 ± 0.09; Manders M1 [*RMRP*→mitochondria] = 0.71 ± 0.11), which was significantly reduced in both DDX5 knockdown (PCC = 0.42 ± 0.12, M1 = 0.38 ± 0.14) and DDX3X knockdown cells (PCC = 0.45 ± 0.15; M1 = 0.42 ± 0.16). To quantitatively assess these changes in mitochondrial *RMRP* content, we isolated mitochondrial fractions from control and knockdown cells, and we measured *RMRP* levels by qPCR (Fig. 6, see *SI Appendix* for details on *Materials and Methods*). Consistent with our FISH experiment observations, mitochondrial *RMRP* levels were significantly reduced following knockdown of either DDX3X (*Top Right* panel, reduced to approximately 50% of control levels) or DDX5 (*Bottom Right* panel, reduced to approximately 25% of control levels). Importantly, these reductions occurred without significant changes in GRSF1 expression in mitochondria (*Left* panels) or mitochondrial content, as measured by MT-$CO_2$ levels (*Bottom Middle* panel), confirming that the observed decrease in mitochondrial *RMRP* represents a specific defect in *RMRP* trafficking.

These findings reveal an unexpected convergence in the roles of DDX5 and DDX3X, with both helicases being essential for maintaining proper mitochondrial localization of *RMRP*, despite their different binding affinities and helicase activities on *RMRP* (Fig. 3).

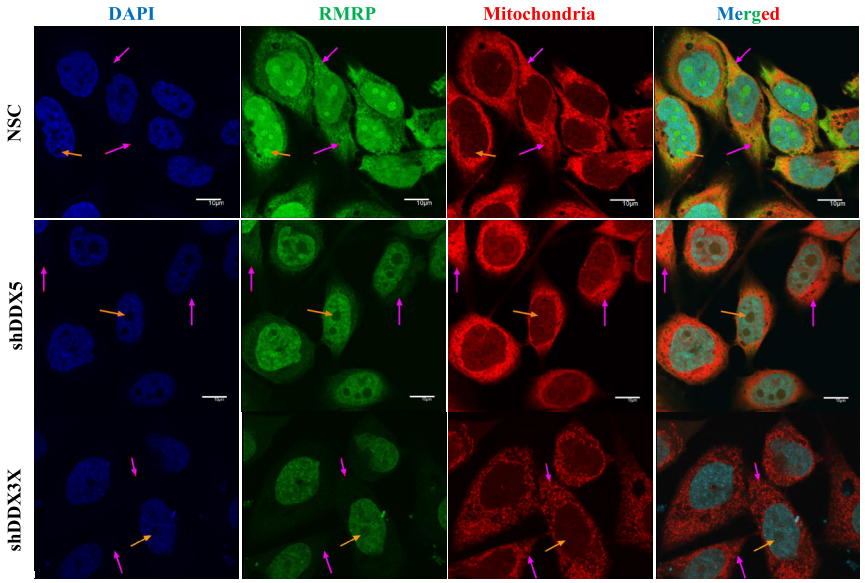


**Fig. 5.** Fluorescence microscopy reveals reduced mitochondrial localization of *RMRP* following DDX5 or DDX3X knockdown. Fluorescence microscopy images of PC-3 M cells showing *RMRP* localization (green, FISH) relative to mitochondria (red, MitoTracker) and nuclei (blue, DAPI) under different conditions. *Top* panel: Control cells (NSC) displaying *RMRP* distribution in both nuclear (purple arrows) and mitochondrial (orange arrows) compartments, with distinct colocalization signals visible in the merged image. *Middle* panel: DDX5 knockdown cells showing reduced mitochondrial localization of *RMRP*, evidenced by decreased yellow-orange colocalization signals (orange arrows) while maintaining some nuclear presence (purple arrows). *Bottom* panel: DDX3X knockdown cells exhibiting reduced *RMRP* signal intensity and diminished mitochondrial localization, accompanied by altered mitochondrial morphology with more fragmented and dispersed patterns. (Scale bar, 10 μm.) These images demonstrate that both DDX5 and DDX3X are required for efficient mitochondrial localization of *RMRP*, suggesting their essential roles in *RMRP* trafficking between cellular compartments.

This suggests that they may function in a cooperative or sequential manner to facilitate *RMRP* trafficking to mitochondria, potentially by promoting specific structural conformations of *RMRP* that are required for mitochondrial import or by participating in the assembly of *RMRP*-containing ribonucleoprotein complexes destined for mitochondria. Previous studies have demonstrated that GRSF1 plays a crucial role in maintaining *RMRP* within mitochondria (13). However, our data suggest that this process also depends on RNA helicases, which may prepare *RMRP* for structural recognition by GRSF1 or for mitochondrial import.

GRSF1 has been characterized as a mitochondrial matrix protein that binds G-rich RNAs and facilitates their localization and function in mitochondria (60). *RMRP* possess a G-rich region that is likely to bind. It is highlighted in our computational models (red, Fig. 1*A*). Our data indicate that even with normal GRSF1 levels, *RMRP* fails to efficiently localize to mitochondria when either DDX5 or DDX3X is depleted, suggesting that these helicases may be required to present *RMRP* in a conformation that is recognizable by GRSF1 or compatible with the mitochondrial import machinery. The altered mitochondrial morphology observed in DDX3X-depleted cells suggests that the proper localization of *RMRP* to mitochondria may be essential for maintaining mitochondrial integrity. This observation aligns with previous studies demonstrating that *RMRP* plays roles in mitochondrial RNA processing and, potentially, in mitochondrial DNA replication (13). The reduction in mitochondrial *RMRP* levels following helicase knockdown may therefore have functional consequences for mitochondrial physiology, potentially contributing to the pathogenesis of disorders associated with *RMRP* dysfunction, such as cartilage-hair hypoplasia and various cancers in which *RMRP* is dysregulated (3, 4).

***RMRP* Depletion Disrupts Mitochondrial Membrane Potential and Increases ROS Production.** Given the reduced mitochondrial localization of *RMRP* following helicase knockdown and altered mitochondrial morphology, we directly investigated the functional consequences of *RMRP* depletion on mitochondrial homeostasis. To comprehensively assess mitochondrial function, we examined

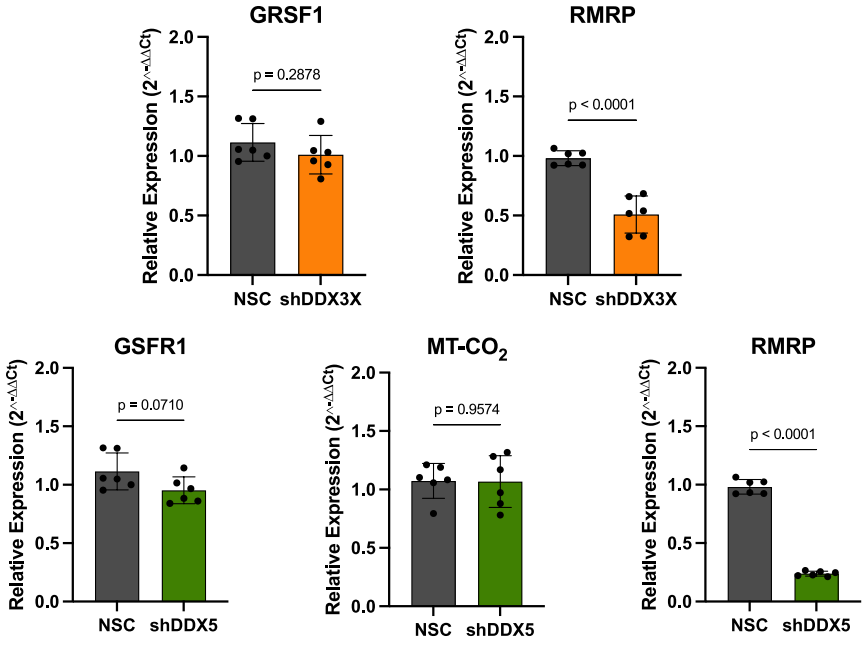


**Fig. 6.** Quantitative analysis confirms a reduction in mitochondrial *RMRP* content following helicase knockdown. qPCR analysis of RNA extracted from isolated mitochondrial fractions of PC-3 M cells. *Top* row: Comparison of GRSF1 (*Left*) and *RMRP* (*Right*) levels in mitochondria from control (NSC) and DDX3X-knockdown cells. DDX3X depletion significantly reduces mitochondrial *RMRP* content to approximately 50% of control levels ($P < 0.0001$) without affecting GRSF1 expression ($P = 0.2878$). *Bottom* row: Comparison of GRSF1 (*Left*), MT-$CO_2$ (*Middle*), and *RMRP* (*Right*) levels in mitochondria from control and DDX5-knockdown cells. DDX5 depletion results in a more pronounced reduction in mitochondrial *RMRP* content, to approximately 25% of control levels ($P < 0.0001$), without significant changes in GRSF1 expression ($P = 0.0710$) or mitochondrial content, as assessed by MT-$CO_2$ levels ($P = 0.9574$). Data are presented as mean ± SD from six independent experiments. Statistical significance was determined by unpaired *t* test comparing each knockdown to its corresponding NSC. These results provide quantitative confirmation that both DDX5 and DDX3X are essential for maintaining normal mitochondrial *RMRP* levels, with DDX5 depletion resulting in a more severe reduction.

multiple parameters in control and *RMRP*-knockdown PC-3 M cells, including mitochondrial morphology, membrane potential, ROS production, apoptosis, and cell proliferation. Visualization of mitochondria using MitoTracker revealed subtle but consistent alterations in mitochondrial network morphology following *RMRP* knockdown (Fig. 7*A*). While control cells (NSC) displayed a well-organized, elongated, and interconnected mitochondrial network, *RMRP*-depleted cells (Δ*RMRP*) showed a more fragmented, circular-shaped, and dispersed mitochondrial pattern, suggesting impaired mitochondrial fusion and network integrity. This morphological change is reminiscent of the alterations observed in cells with dysfunctional mitochondrial dynamics and is consistent with previous reports linking *RMRP* to mitochondrial function (13).

To assess mitochondrial functional integrity, we measured mitochondrial membrane potential using the JC-1 dye, which exhibits potential-dependent accumulation in mitochondria with a shift from green (monomers) to red (aggregates) fluorescence indicating healthy polarized mitochondria (Fig. 7*B*). Quantitative analysis revealed a significant reduction in the red/green fluorescence ratio in *RMRP*-knockdown cells compared to controls (Fig. 7*C*), demonstrating that *RMRP* depletion leads to mitochondrial membrane depolarization. This approximately 35% reduction in membrane potential indicates compromised mitochondrial function. It suggests impaired oxidative phosphorylation, aligning with our GO analysis, which identified oxidative phosphorylation as one of the most significantly enriched pathways associated with *RMRP* (Fig. 2*B*). Mitochondrial membrane depolarization is often associated with increased production of reactive oxygen species (ROS). Accordingly, we measured both cellular and mitochondrial-specific ROS levels. *RMRP*-knockdown cells exhibited significantly elevated levels of both cellular ROS (Fig. 7*D*) and mitochondrial ROS (Fig. 7*E*) compared to control cells. The increase in mitochondrial ROS was particularly pronounced, suggesting that *RMRP* depletion specifically compromises mitochondrial redox homeostasis. These findings provide direct evidence that *RMRP* is essential for maintaining proper mitochondrial redox balance. To further confirm the specific role of ROS in the observed phenotype, we included controls with N-acetylcysteine (NAC, a general antioxidant) and antimycin A (Anti-A, a mitochondrial Complex III inhibitor that induces ROS production). As expected, NAC treatment reduced cellular ROS levels, while antimycin A treatment increased them, validating our ROS detection methodology.

Despite the significant mitochondrial dysfunction and increased ROS production, *RMRP*-knockdown cells showed no significant activation of caspase 3/7 (Fig. 7*F*), suggesting that the level of mitochondrial dysfunction induced by *RMRP* depletion was insufficient to trigger apoptosis under our experimental conditions. Similarly, BrdU incorporation assays revealed no significant difference in cell proliferation between control and *RMRP*-knockdown cells (Fig. 7*G*), indicating that the cells maintain proliferative capacity despite mitochondrial dysfunction. This suggests that PC-3 M cells may adapt to *RMRP*-induced mitochondrial dysfunction by shifting their metabolic dependencies, a hypothesis supported by previous studies linking *RMRP* to metabolic regulation in cancer cells (5–7).

To independently validate our JC-1 membrane potential measurements and rule out dye-specific artifacts, we employed tetramethylrhodamine methyl ester (TMRM) as an orthogonal probe for mitochondrial membrane potential (*SI Appendix*, Fig. S6). TMRM is a lipophilic cationic dye that accumulates in mitochondria in proportion to their membrane potential (61), and we used it in nonquench mode (low concentration, 20 nM) to avoid potential complications from dye aggregation. Confocal microscopy revealed robust TMRM accumulation in mitochondria of control cells, visible as punctate red fluorescence throughout the cytoplasm with characteristic tubular mitochondrial network morphology (*SI Appendix*, Fig. S6*A*). In stark contrast, *RMRP*-knockdown cells displayed markedly reduced TMRM signal intensity with altered mitochondrial morphology appearing more fragmented and dispersed (*SI Appendix*, Fig. S6 *A*, *Bottom* row). Quantitative analysis of integrated TMRM fluorescence, normalized to nuclear count, demonstrated a statistically significant ~43% reduction in *RMRP*-depleted cells compared to controls (*SI Appendix*, Fig. S6*B*). This magnitude of reduction is highly consistent with our JC-1 data (Fig. 7*C*, ~35% reduction), providing strong orthogonal validation. Additionally, we performed real-time kinetic analysis of TMRM fluorescence before and after addition of the mitochondrial uncoupler carbonyl cyanide 4-(trifluoromethoxy)phenylhydrazone (FCCP, 1 μM), which dissipates the proton gradient across the inner mitochondrial membrane by acting as a protonophore (*SI Appendix*, Fig. S6*C*). Both control and *RMRP*-knockdown cells showed the expected spike in TMRM fluorescence immediately upon FCCP addition, followed by a decay as the membrane potential collapses and TMRM exits mitochondria. Quantification of mean fluorescence intensity in the baseline period ("Before", 0 to 60 s) versus the post-FCCP period ("After", 200 to 240 s) revealed that control cells maintained significantly higher membrane potential at baseline (22.0 ± 2.5 A.U.) compared to *RMRP*-knockdown cells (17.2 ± 2.1 A.U., $P = 0.0032$). After FCCP treatment, both conditions showed complete membrane depolarization but were low in *RMRP*-knockdown cells (Control: 17.5 ± 2.8 A.U.; LNA: 10.2 ± 2.4 A.U.; *SI Appendix*, Fig. S6*D*). Since Complex IV is essential for maintaining mitochondrial membrane potential, its disruption leads to a progressive loss of mitochondrial potential, thereby increasing mitochondrial stress, elevating ROS production, and potentially triggering cell death through mPTP opening.

***RMRP* Regulates the Expression of Nuclear-Encoded Mitochondrial Proteins.** To gain mechanistic insights into how *RMRP* influences mitochondrial function, we examined the expression of selected mitochondrial-related genes identified in our *RMRP* pull-down experiments. These included nuclear-encoded mitochondrial proteins involved in different aspects of mitochondrial function: ATP5PO (ATP synthase peripheral stalk subunit), DNAJC11 (mitochondrial import and cristae organization), NDUFS8 (Complex I subunit), and MT-$CO_2$ (mitochondrially encoded cytochrome c oxidase subunit II) as a control for mitochondrial DNA-encoded transcripts. Quantitative PCR analysis revealed differential effects of *RMRP* knockdown on these genes (Fig. 8). Most strikingly, *RMRP* depletion led to significant downregulation of DNAJC11 and NDUFS8, with expression levels reduced to approximately 60% and 45% of control levels, respectively. In contrast, ATP5PO expression remained relatively unaffected, suggesting specificity in *RMRP*'s regulatory effects. Similarly, MT-$CO_2$ levels were unchanged, indicating that mitochondrial DNA content and basic mitochondrial transcription remain intact despite *RMRP* depletion, consistent with our earlier observation that mitochondrial mass was maintained (Fig. 7*C*).

The selective downregulation of DNAJC11 and NDUFS8 provides critical mechanistic insights into how *RMRP* depletion leads to the mitochondrial dysfunction observed in our previous experiments. DNAJC11 is a component of the mitochondrial contact site and cristae organizing system (MICOS) complex, which is essential for maintaining proper cristae morphology and inner membrane organization (62). Its downregulation could explain the altered mitochondrial morphology observed in *RMRP*-depleted cells (Fig. 7*A*), as disruption of cristae structure is known to affect mitochondrial network organization. The substantial reduction

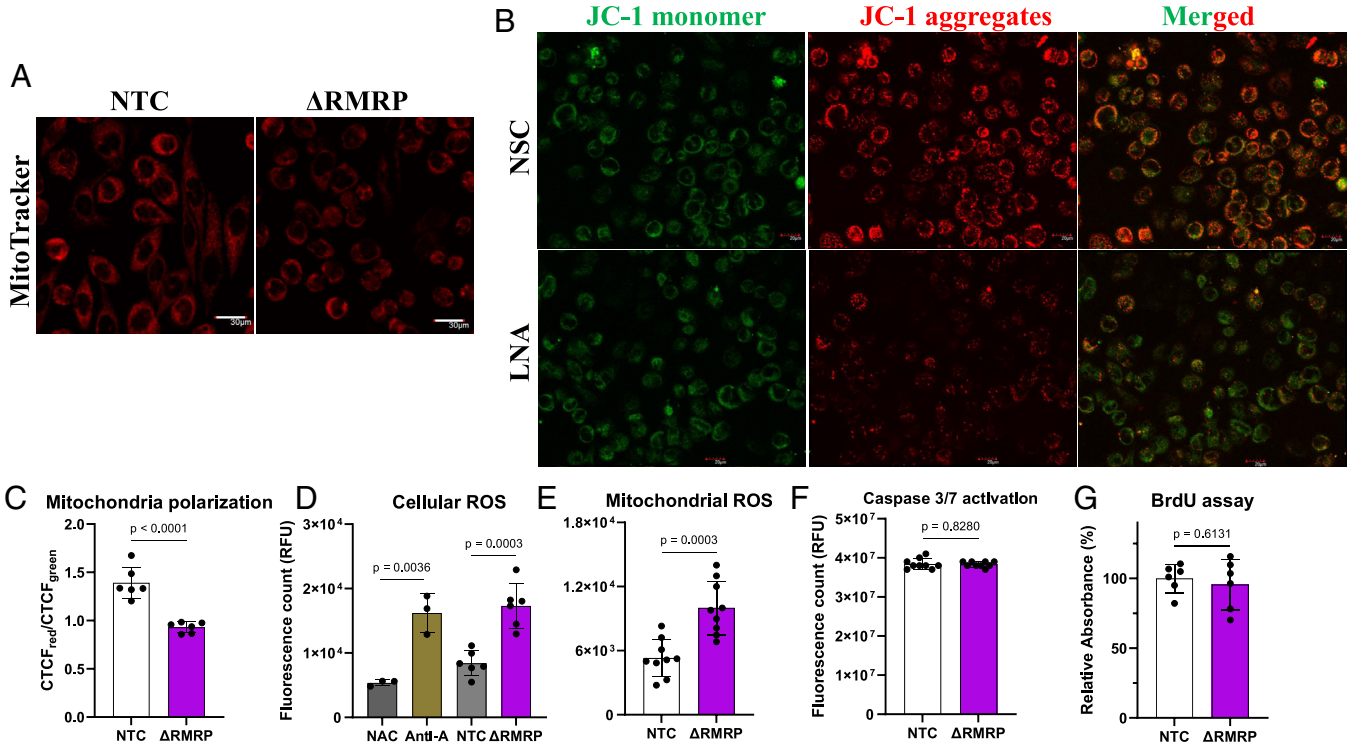


**Fig. 7.** *RMRP* depletion disrupts mitochondrial function and redox homeostasis. (*A*) MitoTracker staining reveals altered mitochondrial morphology in *RMRP*-knockdown (Δ*RMRP*) PC-3 M cells compared to nontargeting control (NTC). *RMRP*-depleted cells show more fragmented and dispersed mitochondrial networks. (Scale bar, 20 μm.) (*B*) JC-1 dye staining for assessment of mitochondrial membrane potential. Green fluorescence indicates JC-1 monomers (depolarized mitochondria), while red fluorescence represents JC-1 aggregates (polarized, healthy mitochondria). *RMRP*-knockdown cells show increased green and reduced red fluorescence compared to controls, indicating mitochondrial depolarization. (*C*) Quantitative analyses of multiple mitochondrial and cellular parameters: *Left* to *Right*: Mitochondrial polarization measured as JC-1 red/green fluorescence ratio, showing significant depolarization in *RMRP*-knockdown cells ($P < 0.0001$); (*D*) Cellular ROS levels measured by DHE fluorescence, with N-acetylcysteine (NAC) and antimycin A (Anti-A) serving as negative and positive controls, respectively, demonstrating elevated ROS in *RMRP*-depleted cells ($P = 0.0003$); (*E*) Mitochondrial-specific ROS measured by MitoSOX, showing increased mitochondrial ROS production in *RMRP*-knockdown cells ($P = 0.0003$); (*F*) Caspase 3/7 activation showing no significant difference between control and *RMRP*-knockdown cells ($P = 0.8280$); (*G*) BrdU incorporation assay showing maintained proliferative capacity in *RMRP*-depleted cells ($P = 0.6131$). Data are presented as mean ± SD from at least six independent measurements. Statistical significance was determined by unpaired *t* test comparing *RMRP* knockdown to NTC. These results establish *RMRP* as a crucial factor in maintaining mitochondrial membrane potential and redox homeostasis, without compromising short-term cell viability or proliferation.

in NDUFS8 expression is particularly significant given its role as an iron-sulfur protein component of respiratory Complex I (NADH: ubiquinone oxidoreductase) (63). Complex I is the largest respiratory chain complex and a significant site for electron entry into the respiratory chain, playing crucial roles in oxidative phosphorylation and maintaining mitochondrial membrane potential (63). Decreased NDUFS8 expression would likely compromise Complex I assembly and function, directly contributing to the mitochondrial membrane depolarization (Fig. 7 *B* and *C*) and increased ROS production (Fig. 7*C*) observed in *RMRP*-knockdown cells. This is consistent with previous studies showing that Complex I dysfunction is a significant source of mitochondrial ROS (64). *RMRP* might function as a scaffold for assembling regulatory complexes that modulate the expression of these genes in response to cellular or mitochondrial signals.

Notably, the genes most affected by *RMRP* knockdown (DNAJC11 and NDUFS8) are involved in fundamental aspects of mitochondrial structure and function, highlighting the critical role of *RMRP* in maintaining mitochondrial homeostasis. The regulatory relationship between *RMRP* and these mitochondrial genes may have broader implications for understanding diseases associated with *RMRP* dysfunction. Cartilage-hair hypoplasia, caused by *RMRP* mutations, affects multiple tissues with high energy demands (65, 66). Our findings suggest that mitochondrial dysfunction, resulting from the dysregulation of key mitochondrial proteins, may contribute to its pathogenesis.

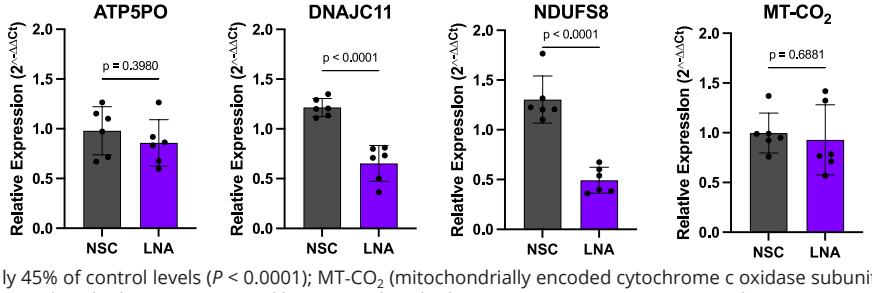


**Fig. 8.** *RMRP* selectively regulates the expression of nuclear-encoded mitochondrial proteins. qPCR analysis of mitochondrial-related gene expression in control (NSC) and *RMRP*-knockdown (LNA) PC-3 M cells. From *Left* to *Right*: ATP5PO (ATP synthase peripheral stalk subunit) shows no significant change in expression following *RMRP* knockdown ($P = 0.3980$); DNAJC11 (mitochondrial import and cristae organization protein) is significantly downregulated to approximately 60% of control levels ($P < 0.0001$); NDUFS8 (NADH: ubiquinone oxidoreductase subunit S8, Complex I component) shows the most pronounced reduction to approximately 45% of control levels ($P < 0.0001$); MT-$CO_2$ (mitochondrially encoded cytochrome c oxidase subunit II) remains unchanged ($P = 0.6881$), indicating preserved mitochondrial DNA content and basic mitochondrial transcription. Data are presented as mean ± SD from six independent experiments. Statistical significance was determined by unpaired *t* test comparing *RMRP* knockdown to NSC. These results demonstrate that *RMRP* selectively regulates nuclear-encoded mitochondrial proteins involved in cristae organization and respiratory chain function, providing a mechanistic explanation for the mitochondrial dysfunction observed in *RMRP*-depleted cells.

***RMRP* Depletion Selectively Impacts OXPHOS Complex Assembly With Pronounced Effects On Complex IV.** To investigate the mechanistic basis for mitochondrial dysfunction observed following *RMRP* depletion, we performed SDS-PAGE to assess the assembly and abundance of oxidative phosphorylation (OXPHOS) Complexes I–V in intact mitochondria isolated from control and *RMRP*-knockdown cells (Fig. 9). SDS-PAGE separates mitochondrial protein complexes based on their molecular weight while preserving their assembled state (67). Analysis of SDS-PAGE revealed differential effects of *RMRP* depletion on individual OXPHOS complexes (Fig. 9*A*). Complex I (NADH: ubiquinone oxidoreductase, ~20 kDa) showed a modest, nonsignificant reduction in *RMRP*-knockdown cells compared to controls. Similarly, Complex II (succinate dehydrogenase, ~30 kDa) and Complex III (cytochrome $bc_1$ complex, ~48 kDa) showed trends toward reduced abundance but did not reach statistical significance. Complex V (ATP synthase, ~55 kDa) remained completely unchanged, indicating that not all OXPHOS complexes are equally affected by *RMRP* depletion.

Strikingly, Complex IV (cytochrome c oxidase, ~40 kDa) showed a significant reduction in *RMRP*-knockdown cells (~32% reduction). This selective effect on Complex IV was unexpected, given our initial focus on NDUFS8 (a Complex I component), but it provides essential mechanistic insight. The selective impact on Complex IV indicates a specific regulatory mechanism rather than generalized mitochondrial stress. Complex IV is the terminal electron acceptor in the respiratory chain and a major contributor to proton pumping and membrane potential maintenance (68). The ~32% reduction in Complex IV abundance we observed is sufficient to explain the mitochondrial membrane depolarization detected by both JC-1 (Fig. 7*C*) and TMRM (*SI Appendix*, Fig. S6) assays.

Complex IV biogenesis is particularly complex, requiring coordinated expression of 13 nuclear-encoded subunits and 3 mitochondrial-encoded subunits (MT-CO1, MT-CO2, MT-CO3), along with numerous assembly factors (69). The preserved MT-CO2 expression in *RMRP*-depleted cells (Fig. 8) suggests that mitochondrial translation is not globally impaired. Instead, the defect likely arises from insufficient nuclear-encoded subunits or assembly factors. While we identified DNAJC11 and NDUFS8 as direct *RMRP* targets, Complex IV assembly may be indirectly affected via DNAJC11, which maintains cristae architecture where respiratory chain supercomplexes assemble (69). DNAJC11 is a component of the mitochondrial contact site and cristae organizing system (MICOS) complex, which shapes cristae junctions and influences the organization of OXPHOS complexes (70, 71). Disrupted cristae structure in *RMRP*-depleted cells could disproportionately affect Complex IV, which is particularly sensitive to membrane architecture and forms respiratory supercomplexes (respirasomes) in the cristae membrane (72).

***RMRP* Depletion Disrupts Mitochondrial Magnesium Homeostasis, Connecting Structure to Cellular Function.** Given the prominent $Mg^{2+}$-dependent structural dynamics of *RMRP* revealed by our SAXS analysis (Fig. 1) and the critical role of $Mg^{2+}$ as a cofactor for numerous mitochondrial enzymes, we investigated whether *RMRP* function influences mitochondrial $Mg^{2+}$ homeostasis. Using the mitochondria-targeted fluorescent indicator KM-301, we measured matrix-free $Mg^{2+}$ levels in live control and *RMRP*-knockdown PC-3 M cells (Fig. 9 *G* and *H*). Confocal microscopy revealed robust KM-301 fluorescence (red) in control cells, with a punctate distribution characteristic of mitochondrial localization. The localization of KM-301-stained mitochondria around the nucleus

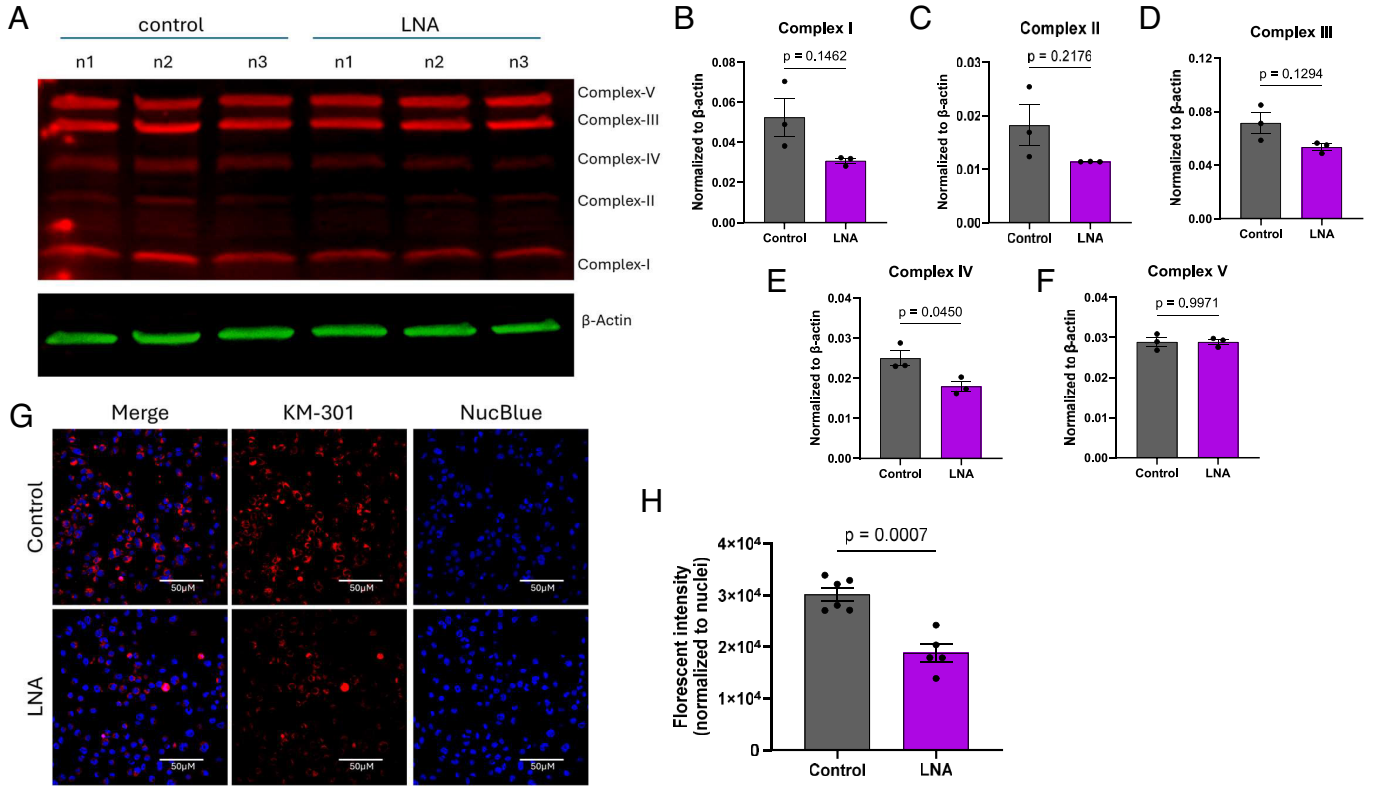


**Fig. 9.** *RMRP* depletion impairs OXPHOS complex assembly, with a selective effect on Complex IV. (*A*) Blue-native polyacrylamide gel electrophoresis (BN-PAGE) analysis of OXPHOS complexes in mitochondria isolated from control (NSC) and RMRP-knockdown (LNA) PC-3 M cells. *Left* panel: Representative BN-PAGE gel stained for total protein (*Top*) with Complexes I–V labeled, and β-actin loading control by conventional SDS-PAGE (*Bottom*). n1, n2, n3 indicate three biological replicates. (*B–F*) *Right* panels: Densitometric quantification of each OXPHOS complex normalized to β-actin. RMRP depletion disrupts mitochondrial $Mg^{2+}$ homeostasis. (*G*) Representative confocal microscopy images of live PC-3 M cells stained with KM-301 (red, mitochondrial $Mg^{2+}$ indicator) and NucBlue (blue, nuclear counterstain) in control (*Top*) and RMRP-knockdown (LNA, *Bottom*) conditions. (Scale bar, 50 μm.) (*H*) Quantification of integrated KM-301 fluorescence normalized to nuclei count.

(NucBlue, blue) exhibits a consistent staining pattern, similar to that of highly specific mitochondrial stains TMRM and JC-1. *RMRP*-knockdown cells showed dramatically reduced KM-301 signal intensity (Fig. 9*G*), indicating lower mitochondrial $Mg^{2+}$ levels. Notably, nuclear NucBlue staining remained unchanged, confirming that the reduction was specific to the mitochondrial $Mg^{2+}$ pool rather than a global cellular effect or loss of cell viability. Quantitative analysis revealed that *RMRP* depletion resulted in a ~37% reduction in mitochondrial $Mg^{2+}$ levels ($P$ = 0.0007; Fig. 9*H*). This striking finding establishes an unexpected connection between *RMRP* function and mitochondrial ion homeostasis, creating a potential feedback loop: *RMRP*'s structure is $Mg^{2+}$-sensitive in vitro (Fig. 1), and *RMRP* depletion disrupts mitochondrial $Mg^{2+}$ homeostasis in cells. This bidirectional relationship suggests that *RMRP* may function as both a $Mg^{2+}$-responsive structural switch and a regulator of $Mg^{2+}$ homeostasis, enabling dynamic coordination of mitochondrial gene expression with metabolic state.

Reduced mitochondrial $Mg^{2+}$ levels could contribute to the observed OXPHOS defects through multiple mechanisms. Several nonmutually exclusive models could explain this phenotype: **Model 1**—Direct *RMRP* involvement in $Mg^{2+}$ transport regulation. *RMRP* might regulate transcription of mitochondrial $Mg^{2+}$ transporters such as MRS2 (the central mitochondrial $Mg^{2+}$ influx channel) or SLC41A3 (a putative $Mg^{2+}$ efflux transporter) (73). While these genes were not identified in our proteomic screen (Fig. 3), *RMRP* could regulate their transcription, consistent with our actinomycin-D data showing *RMRP* acts at the transcriptional level (*SI Appendix*, Fig. S7). **Model 2**—Consequence of bioenergetic dysfunction. Mitochondrial $Mg^{2+}$ levels are tightly coupled to ATP/ADP ratios and membrane potential (74). The reduced OXPHOS capacity (Fig. 9) and membrane depolarization (Fig. 7*B*) in *RMRP*-depleted cells could, in turn, affect $Mg^{2+}$ homeostasis by altering electrochemical gradients or ATP-dependent $Mg^{2+}$ transport. $Mg^{2+}$ uptake into mitochondria via MRS2 is partially electrogenic and therefore sensitive to membrane potential changes (74). **Model 3**—Impaired mitochondrial cristae structure. DNAJC11, which is downregulated in *RMRP*-depleted cells (Fig. 8), is a component of the MICOS complex that organizes cristae junctions. Disrupted cristae architecture could impair $Mg^{2+}$ channel localization or function, as ion channels and transporters are often localized to specific membrane microdomains (75).

The functional consequences of reduced mitochondrial $Mg^{2+}$ are likely substantial and could create a feed-forward cycle of dysfunction. $Mg^{2+}$ is an essential cofactor for ATP synthase, serving both as the $Mg^{2+}$-ATP substrate and as a stabilizer of the enzyme's catalytic site through direct coordination with the γ-phosphate (76). Additionally, multiple TCA cycle dehydrogenases require $Mg^{2+}$ as a cofactor, including isocitrate dehydrogenase and α-ketoglutarate dehydrogenase, and mitochondrial ribosomes are $Mg^{2}$-dependent for structural integrity and function (77). This could create a cycle where reduced mitochondrial protein synthesis further impairs OXPHOS complex assembly beyond the direct transcriptional effects on DNAJC11 and NDUFS8. The $Mg^{2+}$-dependent structural plasticity we observe in vitro (Fig. 1) may have functional relevance in vivo. *RMRP* could adopt different conformations in response to local mitochondrial $Mg^{2+}$ concentrations, potentially influencing its interactions with DDX5, DDX3X, and other regulatory proteins. This structural responsiveness could enable *RMRP* to function as a sensor of mitochondrial metabolic state, adjusting gene expression in response to changing ionic conditions. Such $Mg^{2+}$-responsive structural switches have been described for other RNAs, including riboswitches and catalytic RNAs (78, 79), supporting the biological plausibility of this model. Recent studies have revealed that mitochondrial $Mg^{2+}$ homeostasis is tightly regulated by transporters such as MRS2 and coordinated with ER-mitochondrial $Mg^{2+}$ flux, with important implications for cellular metabolism and stress responses (80–82). Future investigations into how physiological changes in mitochondrial $Mg^{2+}$ dynamics influence *RMRP* conformation and its interactions with protein partners may reveal additional layers of regulation in this system.

## Conclusion

This study provides insights into the structural dynamics and functions of the long noncoding RNA *RMRP*, using biophysical characterization and protein interaction analyses. Our SAXS analysis shows that *RMRP*'s conformation changes with $Mg^{2+}$ concentration, suggesting its functional versatility through modulated protein interactions and subcellular trafficking. We have identified interactions between *RMRP* and the DEAD-box RNA helicases DDX5 and DDX3X, with DDX5 showing high affinity and strong ATP-dependent helicase activity. At the same time, DDX3X displays moderate affinity and minimal activity. Both helicases are crucial for mitochondrial localization of *RMRP*, and their depletion significantly reduces mitochondrial *RMRP* levels. Functionally, *RMRP* is vital for mitochondrial homeostasis; its depletion disrupts mitochondrial morphology and increases ROS production without affecting short-term cell viability. *RMRP* regulates genes involved in mitochondrial function, linking it to diseases such as cartilage-hair hypoplasia and cancer. In conclusion, *RMRP* is a dynamic long noncoding RNA (lncRNA) that interacts with DDX5 and DDX3X to maintain mitochondrial function. These findings enhance our understanding of *RMRP* biology and its association with various pathologies, potentially guiding therapeutic strategies.

## Methodology

A detailed description of all *Materials and Methods* is included in *SI Appendix*, including RNA synthesis and purification, light scattering and X-ray scattering experiments, computational modeling of *RMRP*, pull-down and GO analysis, microscale thermophoresis (MST) and helicase assays, RNA quantification by qPCR, mitochondria-related experiments and cell imaging, FISH, and Immunoblot analysis of OXPHOS complexes.

**Data, Materials, and Software Availability.** We have submitted SAXS data for *RMRP* with buffer containing 5 mM $Mg^{2+}$ and 20 mM $Mg^{2+}$ to SASDBD (https://www.sasbdb.org/project/2779/shk4hjbwfn) (27). *RMRP* IP data: Spreadsheet with raw data and analysis available as a *SI Appendix*.

**ACKNOWLEDGMENTS.** Jason Luddu's undergraduate research work was supported by NSERC USRA, along with NSERC DG Grants awarded to Trushar R. Patel. Zachary Robinson's undergraduate research was supported by NSERC USRA. Trushar R. Patel acknowledges Canada Research Chair, Canada Foundation for Innovation, NSERC Discovery and NSERC Research Tools and Instruments programs. We also thank the DIAMOND beamline (B21) for their support with data collection.

1. J. C. R. Fernandes, S. M. Acuna, J. I. Aoki, L. M. Floeter-Winter, S. M. Muxel, Long non-coding RNAs in the regulation of gene expression: Physiology and disease. *Non-coding RNA* **5**, 17 (2019).
2. A. N. Martin, Y. Li, RNase MRP RNA and human genetic diseases. *Cell Res.* **17**, 219–226 (2007).
3. P. Hermanns *et al.*, Consequences of mutations in the non-coding RMRP RNA in cartilage-hair hypoplasia. *Hum. Mol. Genet.* **14**, 3723–3740 (2005).
4. S. Vakkilainen *et al.*, The human long non-coding RNA gene RMRP has pleiotropic effects and regulates cell-cycle progression at G2. *Sci. Rep.* **9**, 13758 (2019).
5. Q. Meng, M. Ren, Y. Li, X. Song, LncRNA-RMRP acts as an oncogene in lung cancer. *PLoS One* **11**, e0164845 (2016).
6. Y. Chen *et al.*, Inactivation of the tumor suppressor p53 by long noncoding RNA RMRP. *Proc. Natl. Acad. Sci. U.S.A.* **118**, e2026813118 (2021).

7. Y. Huang *et al.*, LncRNA RNA component of mitochondrial RNA-processing endoribonuclease promotes AKT-dependent breast cancer growth and migration by trapping MicroRNA-206. *Front. Cell Dev. Biol.* **9**, 730538 (2021).
8. S. Mattijssen, T. J. Welting, G. J. Pruijn, RNase MRP and disease. *Wiley Interdiscip. Rev. RNA* **1**, 102–116 (2010).
9. P. Lan *et al.*, Structural insight into precursor ribosomal RNA processing by ribonuclease MRP. *Science* **369**, 656–663 (2020).
10. F. Santambrogio, P. Gandellini, G. Cimino-Reale, N. Zaffaroni, M. Folini, MicroRNA-dependent regulation of telomere maintenance mechanisms: A field as much unexplored as potentially promising. *Curr. Pharm. Des.* **20**, 6404–6421 (2014).
11. Y. Dong, T. Yoshitomi, J. F. Hu, J. Cui, Long noncoding RNAs coordinate functions between mitochondria and the nucleus. *Epigenetics Chromatin* **10**, 41 (2017).
12. B. M. Hussen, T. Azimi, H. J. Hidayat, M. Taheri, S. Ghafouri-Fard, Long non-coding RNA RMRP in the pathogenesis of human disorders. *Front. Cell Dev. Biol.* **9**, 676588 (2021).
13. J. H. Noh *et al.*, HuR and GRSF1 modulate the nuclear export and mitochondrial localization of the lncRNA RMRP. *Genes Dev.* **30**, 1224–1239 (2016).
14. S. C. Walker, J. M. Avis, Secondary structure probing of the human RNase MRP RNA reveals the potential for MRP RNA subsets. *Biochem. Biophys. Res. Commun.* **335**, 314–321 (2005).
15. P. Linder, E. Jankowsky, From unwinding to clamping – The DEAD box RNA helicase family. *Nat. Rev. Mol. Cell Biol.* **12**, 505–516 (2011).
16. J. Sun *et al.*, RNA helicase DDX5 enables STAT1 mRNA translation and interferon signalling in hepatitis B virus replicating hepatocytes. *Gut* **71**, 991–1005 (2022).
17. K. Xu *et al.*, *DDX5* and *DDX17*-multifaceted proteins in the regulation of tumorigenesis and tumor progression. *Front. Oncol.* **12**, 943032 (2022).
18. C. S. Ryan, M. Schroder, The human DEAD-box helicase DDX3X as a regulator of mRNA translation. *Front. Cell Dev. Biol.* **10**, 1033684 (2022).
19. F. Li *et al.*, Role of the DEAD-box RNA helicase DDX5 (p68) in cancer DNA repair, immune suppression, cancer metabolic control, virus infection promotion, and human microbiome (microbiota) negative influence. *J. Exp. Clin. Cancer Res.* **42**, 213 (2023).
20. D. R. McGivern, S. M. Lemon, Virus-specific mechanisms of carcinogenesis in hepatitis C virus associated liver cancer. *Oncogene* **30**, 1969–1983 (2011).
21. W. Cheng, G. Chen, H. Jia, X. He, Z. Jing, DDX5 RNA helicases: Emerging roles in viral infection. *Int. J. Mol. Sci.* **19**, 1122 (2018).
22. G. M. Bol, M. Xie, V. Raman, DDX3, a potential target for cancer treatment. *Mol. Cancer* **14**, 188 (2015).
23. N. M. Fischer, M. D. Poleto, J. Steuer, D. van der Spoel, Influence of Na+ and Mg2+ ions on RNA structures studied with molecular dynamics simulations. *Nucleic Acids Res.* **46**, 4872–4882 (2018).
24. S. Somarowthu *et al.*, HOTAIR forms an intricate and modular secondary structure. *Mol. Cell* **58**, 353–361 (2015).
25. F. Liu, S. Somarowthu, A. M. Pyle, Visualizing the secondary and tertiary architectural domains of lncRNA RepA. *Nat. Chem. Biol.* **13**, 282–289 (2017).
26. D. N. Kim *et al.*, Zinc-finger protein CNBP alters the 3-D structure of lncRNA Braveheart in solution. *Nat. Commun.* **11**, 148 (2020).
27. H. S. Pereira, T. R. Patel, Human lncRNA RMRP interacts with DEAD-box helicases and modulates mitochondrial function. SASBDB. https://www.sasbdb.org/project/2779/shk4hjbwfn. Deposited 19 December 2025.
28. R. Aguilar *et al.*, Targeting Xist with compounds that disrupt RNA structure and X inactivation. *Nature* **604**, 160–166 (2022).
29. M. H. D'Souza *et al.*, Biophysical characterisation of human LincRNA-p21 sense and antisense Alu inverted repeats. *Nucleic Acids Res.* **50**, 5881–5898 (2022).
30. T. Mrozowich *et al.*, Investigating RNA–RNA interactions through computational and biophysical analysis. *Nucleic Acids Res.* **51**, 4588–4601 (2023).
31. D. Grilley, A. M. Soto, D. E. Draper, Mg2+–RNA interaction free energies and their relationship to the folding of RNA tertiary structures. *Proc. Natl. Acad. Sci. U.S.A.* **103**, 14003–14008 (2006).
32. D. Leipply, D. E. Draper, Dependence of RNA tertiary structural stability on Mg2+ concentration: Interpretation of the Hill equation and coefficient. *Biochemistry* **49**, 1843–1853 (2010).
33. L. E. Rogler *et al.*, Small RNAs derived from lncRNA RNase MRP have gene-silencing activity relevant to human cartilage-hair hypoplasia. *Hum. Mol. Genet.* **23**, 368–382 (2014).
34. A. M. Mustoe, N. N. Lama, P. S. Irving, S. W. Olson, K. M. Weeks, RNA base-pairing complexity in living cells visualized by correlated chemical probing. *Proc. Natl. Acad. Sci. U.S.A.* **116**, 24574–24582 (2019).
35. C. Yin, G. Bai, Y. Zhang, J. Huang, Crystal structure of human RPP20–RPP25 proteins in complex with the P3 domain of lncRNA RMRP. *J. Struct. Biol.* **213**, 107704 (2021).
36. H. L. Cao, Z. J. Liu, P. L. Huang, Y. L. Yue, J. N. Xi, lncRNA-RMRP promotes proliferation, migration and invasion of bladder cancer via miR-206. *Eur. Rev. Med. Pharmacol. Sci.* **23**, 1012–1021 (2019).
37. N. Robertson *et al.*, A disease-linked lncRNA mutation in RNase MRP inhibits ribosome synthesis. *Nat. Commun.* **13**, 649 (2022).
38. J. Pan, D. Zhang, J. Zhang, P. Qin, J. Wang, LncRNA RMRP silence curbs neonatal neuroblastoma progression by regulating microRNA-206/tachykinin-1 receptor axis via inactivating extracellular signal-regulated kinases. *Cancer Biol. Ther.* **20**, 653–665 (2019).
39. N. Zhou, Z. He, H. Tang, B. Jiang, W. Cheng, LncRNA RMRP/miR-613 axis is associated with poor prognosis and enhances the tumorigenesis of hepatocellular carcinoma by impacting oncogenic phenotypes. *Am. J. Transl. Res.* **11**, 2801–2815 (2019).
40. T. Xu *et al.*, Pathological bases and clinical impact of long noncoding RNAs in prostate cancer: A new budding star. *Mol Cancer* **17**, 103 (2018).
41. B. Lee, A. G. Matera, D. C. Ward, J. Craft, Association of RNase mitochondrial RNA processing enzyme with ribonuclease P in higher ordered structures in the nucleolus: A possible coordinate role in ribosome biogenesis. *Proc. Natl. Acad. Sci. U.S.A.* **93**, 11471–11476 (1996).
42. E. McShane *et al.*, A kinetic dichotomy between mitochondrial and nuclear gene expression processes. *Mol. Cell* **84**, 1541–1555.e1511 (2024).
43. K. Anthony, J. M. Gallo, Aberrant RNA processing events in neurological disorders. *Brain Res.* **1338**, 67–77 (2010).
44. F. A. Bustamante-Barrientos *et al.*, Mitochondrial dysfunction in neurodegenerative disorders: Potential therapeutic application of mitochondrial transfer to central nervous system-residing cells. *J. Transl. Med.* **21**, 613 (2023).
45. Y. J. Choi, S. G. Lee, The DEAD-box RNA helicase DDX3 interacts with DDX5, co-localizes with it in the cytoplasm during the G2/M phase of the cycle, and affects its shuttling during mRNP export. *J. Cell. Biochem.* **113**, 985–996 (2012).
46. H. Song, X. Ji, The mechanism of RNA duplex recognition and unwinding by DEAD-box helicase DDX3X. *Nat. Commun.* **10**, 3085 (2019).
47. M. Secchi, C. Lodola, A. Garbelli, S. Bione, G. Maga, DEAD-box RNA helicases DDX3X and DDX5 as oncogenes or oncosuppressors: A network perspective. *Cancers (Basel)* **14**, 3820 (2022).
48. C. Nelson, T. Mrozowich, D. L. Gemmill, S. M. Park, T. R. Patel, Human DDX3X unwinds Japanese encephalitis and Zika viral 5′ terminal regions. *Int. J. Mol. Sci.* **22**, 413 (2021).
49. D. L. Gemmill *et al.*, The 3′ terminal region of Zika virus RNA contains a conserved G-quadruplex and is unfolded by human DDX17. *Biochem. Cell Biol.* **102**, 96–105 (2024).
50. Z. Yu *et al.*, DDX5 resolves R-loops at DNA double-strand breaks to promote DNA repair and avoid chromosomal deletions. NAR. *Cancer* **2**, zcaa028 (2020).
51. Z. Xing, W. K. Ma, E. J. Tran, The DDX5/Dbp2 subfamily of DEAD-box RNA helicases. *WIREs RNA* **10**, e1519 (2019).
52. Y. Toyama, I. Shimada, NMR characterization of RNA binding property of the DEAD-box RNA helicase DDX3X and its implications for helicase activity. *Nat. Commun.* **15**, 3303 (2024).
53. Y. Toyama, K. Takeuchi, I. Shimada, Regulatory role of the N-terminal intrinsically disordered region of the DEAD-box RNA helicase DDX3X in selective RNA recognition. *Nat. Commun.* **16**, 7762 (2025).
54. Z. Xing, S. Wang, E. J. Tran, Characterization of the mammalian DEAD-box protein DDX5 reveals functional conservation with *S. cerevisiae* ortholog Dbp2 in transcriptional control and glucose metabolism. *RNA* **23**, 1125–1138 (2017).
55. V. Tripathi *et al.*, The nuclear-retained noncoding RNA MALAT1 regulates alternative splicing by modulating SR splicing factor phosphorylation. *Mol. Cell* **39**, 925–938 (2010).
56. H. Choi *et al.*, Targeting DDX3X triggers antitumor immunity via a dsRNA-mediated tumor-intrinsic type I interferon response. *Cancer Res.* **81**, 3607–3620 (2021).
57. M. Camats, S. Guil, M. Kokolo, M. Bach-Elias, P68 RNA helicase (DDX5) alters activity of *cis*- and *trans*-acting factors of the alternative splicing of H-Ras. *PLoS One* **3**, e2926 (2008).
58. A. Kar *et al.*, RNA helicase p68 (DDX5) regulates tau exon 10 splicing by modulating a stem-loop structure at the 5′ splice site. *Mol. Cell. Biol.* **31**, 1812–1821 (2011).
59. M. Kokolo, M. Bach-Elias, P68 RNA helicase (DDX5) required for the formation of various specific and mature miRNA active RISC complexes. *Microrna* **11**, 36–44 (2022).
60. A. A. Jourdain *et al.*, GRSF1 regulates RNA processing in mitochondrial RNA granules. *Cell Metab.* **17**, 399–410 (2013).
61. D. Stockarova, M. Hajek, L. Vykus, Laparotomy wound rupture–comments on therapeutic tactics. *Rozhl. Chir.* **65**, 173–177 (1986).
62. T. Stephan *et al.*, MICOS assembly controls mitochondrial inner membrane remodeling and crista junction redistribution to mediate cristae formation. *EMBO J.* **39**, e104105 (2020).
63. M. L. Taddei *et al.*, Mitochondrial oxidative stress due to complex I dysfunction promotes fibroblast activation and melanoma cell invasiveness. *J. Signal Transduct.* **2012**, 684592 (2012).
64. F. Basit *et al.*, Mitochondrial complex I inhibition triggers a mitophagy-dependent ROS increase leading to necroptosis and ferroptosis in melanoma cells. *Cell Death Dis.* **8**, e2716 (2017).
65. P. Hermanns *et al.*, RMRP mutations in cartilage-hair hypoplasia. *Am. J. Med. Genet. A.* **140**, 2121–2130 (2006).
66. X. Sun *et al.*, Rmrp mutation disrupts chondrogenesis and bone ossification in zebrafish model of cartilage-hair hypoplasia via enhanced Wnt/beta-catenin signaling. *J. Bone Miner. Res.* **34**, 2101–2116 (2019).
67. I. Wittig, H. P. Braun, H. Schagger, Blue native PAGE. *Nat. Protoc.* **1**, 418–428 (2006).
68. H. Michel, The mechanism of proton pumping by cytochrome c oxidasex127e [comments]. *Proc. Natl. Acad. Sci. U.S.A.* **95**, 12819–12824 (1998).
69. E. Fernandez-Vizarra, M. Zeviani, Mitochondrial disorders of the OXPHOS system. *FEBS Lett.* **595**, 1062–1106 (2021).
70. F. Wollweber, K. von der Malsburg, M. van der Laan, Mitochondrial contact site and cristae organizing system: A central player in membrane shaping and crosstalk. *Biochim. Biophys. Acta Mol. Cell Res.* **1864**, 1481–1489 (2017).
71. G. S. Williams, L. Boyman, A. C. Chikando, R. J. Khairallah, W. J. Lederer, Mitochondrial calcium uptake. *Proc. Natl. Acad. Sci. U.S.A.* **110**, 10479-10486 (2013).
72. J. A. Letts, K. Fiedorczuk, L. A. Sazanov, The architecture of respiratory supercomplexes. *Nature* **537**, 644–648 (2016).
73. L. Mastrototaro, A. Smorodchenko, J. R. Aschenbach, M. Kolisek, G. Sponder, Solute carrier 41A3 encodes for a mitochondrial Mg(2+) efflux system. *Sci. Rep.* **6**, 27999 (2016).
74. M. Kolisek *et al.*, Mrs2p is an essential component of the major electrophoretic Mg2+ influx system in mitochondria. *EMBO J.* **22**, 1235–1244 (2003).
75. J. Yu *et al.*, Mitochondrial cristae remodeling: Mechanisms, functions, and pathology. *Cell Insight* **4**, 100285 (2025).
76. Y. H. Ko, S. Hong, P. L. Pedersen, Chemical mechanism of ATP synthase. Magnesium plays a pivotal role in formation of the transition state where ATP is synthesized from ADP and inorganic phosphate. *J. Biol. Chem.* **274**, 28853–28856 (1999).
77. D. De Silva, Y. T. Tu, A. Amunts, F. Fontanesi, A. Barrientos, Mitochondrial ribosome assembly in health and disease. *Cell Cycle* **14**, 2226–2250 (2015).
78. R. L. Hayes *et al.*, Magnesium fluctuations modulate RNA dynamics in the SAM-I riboswitch. *J. Am. Chem. Soc.* **134**, 12043–12053 (2012).
79. H. Zheng, I. G. Shabalin, K. B. Handing, J. M. Bujnicki, W. Minor, Magnesium-binding architectures in RNA crystal structures: Validation, binding preferences, classification and motif detection. *Nucleic Acids Res.* **43**, 3789–3801 (2015).
80. C. C. Daw *et al.*, Lactate elicits ER-mitochondrial Mg(2+) dynamics to integrate cellular metabolism. *Cell* **183**, 474–489.e417 (2020).
81. T. R. Madaris *et al.*, Limiting Mrs2-dependent mitochondrial Mg(2+) uptake induces metabolic programming in prolonged dietary stress. *Cell Rep.* **42**, 112155 (2023).
82. N. Vishnu *et al.*, ERMA (TMEM94) is a P-type ATPase transporter for Mg(2+) uptake in the endoplasmic reticulum. *Mol. Cell* **84**, 1321–1337.e1311 (2024).